Received: 30 March 2017 | Revised: 17 June 2017 | Accepted: 26 June 2017
DOI: 10.1002/pip.2920

WILEY PROGRESS IN PHOTOVOLTAICS

RESEARCH ARTICLE

Colloidal quantum dot solar cell power conversion efficiency optimization using analysis of current-voltage characteristics and electrode contact imaging by lock-in carrierography

Lilei Hu[1] | Mengxia Liu[2] | Andreas Mandelis[1,2] | Alexander Melnikov[1] | Edward H. Sargent[2]

[1] Center for Advanced Diffusion-Wave and Photoacoustic Technologies (CADIPT), Department of Mechanical and Industrial Engineering, University of Toronto, Toronto, ON M5S 3G8, Canada

[2] Edward S. Rogers Sr. Department of Electrical and Computer Engineering, University of Toronto, Toronto, ON M5S 3G4, Canada

Correspondence
Andreas Mandelis, Center for Advanced Diffusion-Wave and Photoacoustic Technologies (CADIPT), Department of Mechanical and Industrial Engineering, University of Toronto, Toronto, ON M5S 3G8, Canada.
Email: mandelis@mie.utoronto.ca

Funding information
Natural Sciences and Engineering Research Council of Canada; Canada Research Chairs

Abstract

Although the power conversion efficiency (PCE) of colloidal quantum dot solar cells (CQDSCs) has increased sharply, researchers are struggling with the lack of comprehensive device efficiency optimization strategies, which retards significant progress in CQDSC improvement. This paper addresses this critical issue through analyzing the impact of colloidal quantum dot (CQD) carrier hopping mobility, bandgap energy, illumination intensity, and electrode/CQD interface on device performance to develop a guiding criterion for CQDSC PCE optimization. This general strategy has been used for the successful fabrication of high-efficiency CQDSCs yielding certified PCEs as high as 11.28 %. A major experimental finding of this work is that the widely used constant photocurrent density (J_{ph}) assumption is invalid as J_{ph} is external-voltage dependent due to the low carrier hopping mobility. Furthermore, the theoretical model developed herein predicts the nonmonotonic dependence of CQDSC PCE on carrier hopping mobility and bandgap energy, which were also demonstrated with the high-efficiency CQDSCs. These results constitute a revision basis of the widespread belief that higher mobility and lower bandgap energy correspond to a higher CQDSC efficiency. Furthermore, electrode/CQD interface-dependent surface recombination velocities were investigated in the framework of our abovementioned theoretical model using lock-in carrierography, a contactless, large-area frequency-domain photocarrier diffusion-wave imaging methodology that elucidated the carrier collection process at the electrodes through open-circuit voltage distribution imaging. Lock-in carrierography eliminates the limitations of today's widely used small-spot (<0.1 cm^2) testing methods which, however, raise questionable overall solar cell performance and stability estimations.

KEYWORDS

bandgap energy, colloidal quantum dot solar cell, electrode-semiconductor interface, hopping mobility, large-area imaging, lock-in carrierography

1 | INTRODUCTION

Colloidal quantum dot solar cells (CQDSCs) are presently attracting immense research interest on a global scale due to the meteoric rise of their solar to electric power conversion efficiency (PCE) from 3% to 13.4% within a period of only 7 years.[1] Intensive efforts are underway to boost CQDSC PCE through device architecture engineering,[2-4] surface materials chemistry,[5-7] synthesis methodologies,[8,9] charge carrier dynamics,[10-17] and theoretical modeling.[18-20] However, no comprehensive device efficiency optimization strategies have been reported aiming at achieving higher PCE, specifically for CQDSCs. Researchers use common sense approaches instead, trying to improve CQDSC efficiency through pursuing higher carrier mobility using disparate surface passivation materials and increasing quantum dot size for lower bandgap energy to harvest the solar spectrum in a wider wavelength range. This universal strategy, however, is typically valid for conventional solar cells of high carrier mobility such as Si solar cells, rather than for low carrier mobility systems of a discrete carrier transport nature, such as colloidal quantum dot (CQD) and organic solar cells. Alarmingly, however, it has been reported that state-of-the-art high PCE solar cells are actually achieved using materials generally not exhibiting the highest CQD carrier mobility.[21] Furthermore, researchers reverted to using smaller dots with wider bandgap energy when they found larger dots yielded even lower PCE. This raises the crucial question of whether higher mobility and smaller bandgap CQDs can always produce higher PCEs in CQDSCs. How do CQD carrier mobility and bandgap energy determine solar cell performance?

The present study addresses these critical issues. With our fabrication and study of CQDSCs that have a certified PCE as high as 11.28 % through a structure shown in Figure 1A, we discovered that the photocurrent density is voltage dependent and is accompanied by low carrier mobilities, which indicates that the conventional constant photocurrent assumption may be invalid for CQDSCs. Generally, to analyze current-voltage characteristics of CQDSCs, the well-known Shockley–Queisser (S-Q) equation is often used,[22] which takes on the form $J_{illu}(V) = J_0\left\{exp\left[\frac{qV_{ext}}{n_{id}k_BT}\right]-1\right\}-J_{ph}$, where J_{illu} is the current density under light illumination, J_0 the saturation current density, J_{ph} a photocurrent density often treated as a constant short-circuit current density, n_{id} the ideality factor, k_B the Boltzmann constant, q the elementary charge, T the absolute temperature, and V_{ext} the externally applied voltage. This equation was derived to model diode behavior in an electrical circuit under the assumption of infinitely large material conductivity (or carrier mobility), which is true for most solid-state p-n junctions such as, Ge, Si, or GaAs. With high carrier mobilities on the order of 10^2 to 10^3 cm^2/Vs for typical Si solar cells, it is true that the photocurrent density J_{ph} is constant through the entire applied voltage range; however, today's CQD-based materials and devices feature multiple energy disorder sources due to their high surface-to-volume ratio nanostructures, variations in confinement energy and coupling, and thermal broadening. All of these point to a noncontinuous hopping/tunneling transport with low mobilities ranging from 10^{-5} to 10^{-1} cm^2/Vs[6,16,18,23-28] for PbS CQDs passivated with various ligands. This huge difference in mobilities leads to questioning the validity of applying the S-Q model to such systems. The discovery of external-voltage-dependent photocurrent density in PbS CQD-based solar cells enabled us to revisit and relax the constant photocurrent density assumption in the well-known S-Q equation for CQDSCs, which has been and continues to be the prevailing assumption among researchers to date. A similar voltage-dependent photocurrent was also reported by Würfel et al[29] for organic solar cells that also have much lower carrier mobility. Therefore, with the derivation of an improved carrier hopping drift-diffusion equation, this study, for the first time, develops a comprehensive analysis of the dependence of CQDSC current-voltage characteristics on carrier mobility and CQD bandgap energy. Contrary to the common sense expectation that higher mobility and lower bandgap energy correspond to a better CQDSC efficiency, reality is more complex, and carrier hopping mobility and bandgap energy optimization is a significant challenge that can be addressed using the methodology presented in this study.

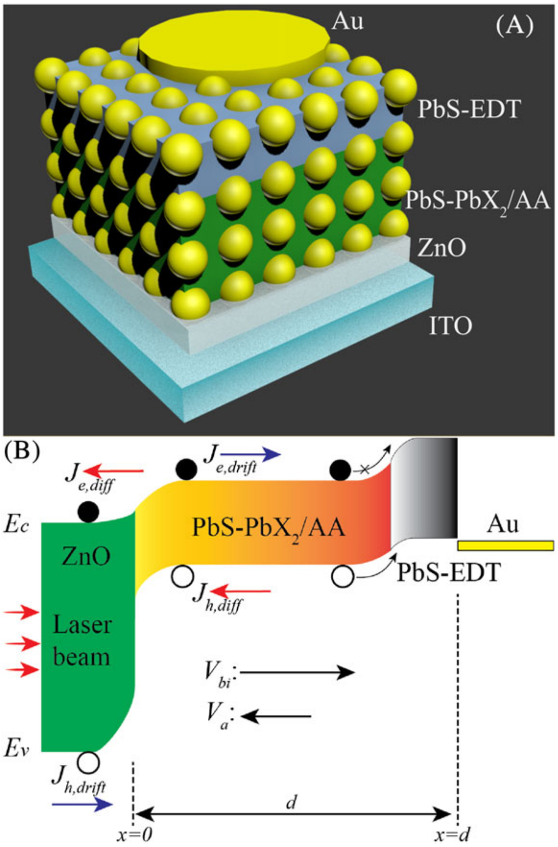

FIGURE 1 **A,** Schematic of colloidal quantum dot solar cell sandwich structure and B, the corresponding energy band structure. PbX$_2$, AA, and EDT represent lead halide, ammonium acetate, and 1,2-ethanedithiol, respectively, acting as exchange-ligands for PbS colloidal quantum dots (CQDs). PbS-EDT CQD layer is used for preventing electrons from diffusing toward Au electrode [Colour figure can be viewed at wileyonlinelibrary.com]

Furthermore, most researchers have reported solar cell efficiencies based on small-spot (<0.1 cm^2) testing, including professional certification characterizations of solar cells towards an entry in the solar cell efficiency tables. This, however, raises questions about the overall solar cell performance and stability estimations. To address this universal problem for CQDSCs, we introduce a large-area photovoltaic device nondestructive imaging (NDI) carrier-diffusion-wave characterization technique that can meet demands for industrial photovoltaic system quality control. The inspection of the entire solar cell area or some specific regions can also fulfill various other purposes such as overall device performance, shading effects, electrical, and/or mechanical defects. Solar cell large-area imaging has been used intensively with perovskite solar cells using camera-based photoluminescence,[30] series resistance imaging using electroluminescence,[31] lock-in thermography (LIT),[32] lock-in carrierography (LIC) characterization of Si wafers,[33-35] and solar cells.[35-38] However, to the best of our knowledge, no imaging studies of CQDSCs have been reported in efforts to acquire an insightful physical picture of defect or contact effects on key solar cell performance parameters. Therefore, we implemented LIC imaging to obtain open-circuit voltage distribution and carrier collection efficiency images and were thus able to elucidate the effects of the CQD/electrode interfaces on solar cell performance within the framework of our drift-diffusion *J-V* model.

With the precedent of the next-generation efficiencies as high as 11.28 % that have been fabricated in our labs and certified as shown in the well-referenced solar cell efficiency tables,[1] the present theoretical model and large-area characterization technique can be of significance for guiding CQDSC optimization with respect to CQD surface passivation ligand selection and the determination of CQD energy bandgap (or quantum dot size), as well as for solar cell fabrication quality control.

2 | DERIVATION OF CARRIER HOPPING DRIFT-DIFFUSION J-V MODEL FOR CQDSCs

Disorder sources in CQD ensembles, including variations in confinement energy, electron-electron repulsion, coupling, and thermal broadening, cause CQD-based materials and devices to exhibit discrete hopping conductivity and diffusivity.[39,40] Using intensity-modulated illumination, the distribution and hopping transport of excitons and charge carriers follows a diffusion-wave behavior. The theory of particle-population-gradient-induced diffusive transport through spatial profiles of discrete hopping into and out of a quantum dot was developed in detail by Mandelis et al.[20] In this paper, the prevailing assumption of constant photocurrent[20] was relaxed. Based on the photocarrier hopping diffusion-wave theory to solve the carrier population rate equation, quenching and surface recombination velocity (SRV) associated boundary conditions were assumed with respect to both hopping diffusion and drift current densities for high-efficiency CQDSC structures, thus overcoming the voltage limitation[20] that leads to a decreased J with V when the applied voltage is higher than the built-in potential. Specifically, in a 1-dimensional quantum dot ensemble, each quantum dot characterized by its own size and energy manifold is separated by a mean distance from its neighbors. Therefore, the rate equation for the net carrier flux entering one quantum dot within a time interval dt can be written as[20]:

$$\frac{\partial n_{PV}(x,t)}{\partial t} = -\frac{\partial J_e(x,t)}{\partial x} - \frac{n_{PV}(x,t)}{\tau}, \tag{1}$$

where $n_{PV}(x)$ is the carrier concentration under illumination, τ is the lifetime, and $J_e(x,t)$ is the carrier hopping flux in units of $s^{-1}cm^{-2}$. The subscript PV indicates that the solar cell is under external bias. With an applied dc voltage, n_{PV} becomes time-independent, therefore, Equation 1 can be further written as

$$\frac{d^2 n_{PV}(x)}{dx^2} - \left(\frac{\mu_e E}{D_e}\right)\frac{dn_{PV}(x)}{dx} - \frac{n_{PV}(x)}{D_e \tau} = 0 \tag{2}$$

where $E = \frac{V_{bi} - V_a}{d}$ is the electric field across the solar cell, d is the CQD thin film thickness as shown in Figure 1B, D_e is the carrier hopping diffusivity, μ_e is the hopping mobility, V_{bi} is the built-in voltage, and V_a is the photovoltage. Equation 2 is subject to a surface boundary condition at $x = 0$ as shown in Figure 1B: $n_{PV}(0) - n(0) = \Delta N_0$, where ΔN_0 is the excess carrier population generated by the photovoltaic effect. A second (quenching) boundary condition for the CQD thin films at $x = d$ is $n_{PV}(d) - n(d) = 0$, indicating an infinite SRV and the immediate recombination of electrons and holes when they drift or diffuse to the interface. Therefore, solving Equation 2 with $\Delta n_{PV}(x) = n_{PV}(x) - n(x)$, it can be found that

$$\Delta n_{PV}(x) = \frac{\Delta N_0\left(e^{Q_2 d + Q_1 x} - e^{Q_1 d + Q_2 x}\right)}{e^{Q_2 d} - e^{Q_1 d}}. \tag{3}$$

The excess carrier population $\Delta N_0 = n(0)\left(e^{\frac{\mu_e V_a}{D_e}} - 1\right)$ can be derived through integrating the electric field over the thickness of a solar cell under both dark and illumination conditions.[20] Accordingly, the hopping drift and diffusion current densities [A/cm^2] can be expressed as

$$\begin{aligned} J_{e,diff} &= -qD_e \frac{d\Delta n_{PV}(x)}{dx}\bigg|_{x=0} \\ &= -qD_e n(0)\left(\frac{Q_1 e^{Q_2 d} - Q_2 e^{Q_1 d}}{e^{Q_2 d} - e^{Q_1 d}}\right)\left(e^{\frac{\mu_e V_a}{D_e}} - 1\right), \end{aligned} \tag{4}$$

$$J_{e,drift} = q\mu_e E n(0)\left(e^{\frac{\mu_e V_a}{D_e}} - 1\right) = q\mu_e\left(\frac{V_{bi} - V_a}{d}\right)n(0)\left(e^{\frac{\mu_e V_a}{D_e}} - 1\right), \tag{5}$$

with

$$Q_{1,2} = \frac{1}{2}\left(C_0 \pm \sqrt{C_0^2 + 4C_1}\right) \tag{6}$$

and with the definitions

$$C_0 = \frac{\mu_e E}{D_e} = \left(\frac{\mu_e}{D_e}\right)\frac{V_{bi} - V_a}{d}, C_1 = \frac{1}{L_e^2}, \tag{7}$$

where L_e is the dc hopping diffusion length. Eventually, the total dark current density J_e (A/cm^2) including drift and diffusion components can be expressed as

$$\begin{aligned} J_e &= J_{e,diff} + J_{e,drift} \\ &= qn(0)\left[-D_e\left(\frac{Q_1 e^{Q_2 d} - Q_2 e^{Q_1 d}}{e^{Q_2 d} - e^{Q_1 d}}\right) + \mu_e\left(\frac{V_{bi} - V_a}{d}\right)\right]\left(e^{\frac{\mu_e V_a}{D_e}} - 1\right). \end{aligned} \tag{8}$$

Therefore, through adding electron and hole dark current densities and considering the photocurrent density, the total carrier hopping current density under illumination can be expressed as usual by

$$J_{illu} = J_e + J_h - J_{ph}. \tag{9}$$

It should be noted that the hopping drift current density J_{drift} is V_a dependent. Specifically, the electric field $\left(\frac{V_{bi} - V_a}{d}\right)$ leads to J_{drift} decreasing with V_a, while the excess carrier population $n(0)e^{\frac{\mu_e V_a}{D_e}}$ yields an exponential dependence of J_{drift} on V_a.

In general, the boundary condition at $x=d$ is not always an infinite SRV. There are four types of surface recombination, namely, minority carrier hole recombination at the cathode, majority carrier hole recombination at the anode, minority carrier electron recombination at the anode, and majority carrier electron recombination at the cathode. Here, however, for the sake of simplification, all types of surface recombination are treated in the same manner. The surface recombination rate at d can be defined as

$$J(d) = S(d)n_{PV}(d) \tag{10}$$

$J(d)$ is a carrier flux in units of $s^{-1}cm^{-2}$. Solving Equation 2 subject to the boundary condition Equation 10, the total current density J_e (A/cm^2) is given by

$$J_e = qn(0)\{-D_e[Q_1 - (Q_1 - Q_2)f] + \mu_e E\}\left(e^{\frac{\mu_e V_a}{D_e}} - 1\right), \tag{11}$$

with the definition

$$f \equiv \frac{e^{Q_1 d}\left[S(d) - \mu_e E + D_e Q_1\right]}{\left[S(d) - \mu_e E\right]\left(e^{Q_1 d} - e^{Q_2 d}\right) + D_e\left(Q_1 e^{Q_1 d} - Q_2 e^{Q_2 d}\right)}. \tag{12}$$

Smaller surface recombination velocity S means more excess charge carriers across the interface which should result in better solar cell performance and $S = 0$ corresponds to Ohmic contact behavior as reported by Kirchartz et al.[41] Also, they found that surface recombination played the role of a carrier recombination source in the way that a zero surface recombination rate precludes carrier recombination at the contacts (interface), while an infinite recombination rate adds a new recombination pathway, leading to strongly decreased V_{oc} and PCE at high carrier mobilities when carrier recombination is significantly increased.

3 | SOLAR CELL FABRICATION AND EFFICIENCY OPTIMIZATION

The synthesis of oleic-acid-capped CQDs and ZnO nanoparticles follows our previously published methods.[42] Figure 1A shows the sandwich structure of the CQDSCs under study. ZnO nanoparticles in solution were spin casted onto an ITO glass at 3000 rpm for 20 seconds, which was followed by the deposition of PbS CQDs using PbX_2/AA-exchanged (PbX_2: lead halide, AA: ammonium acetate) PbS inks.[43] In addition, 2 EDT(1,2-ethanedithiol)-exchanged PbS CQD layers were spin-coated atop the previous PbS CQD layers. Eventually, a 120-nm thin Au film was thermally evaporated to form the top electrode.

Following the device efficiency optimization strategy (see section 4.2) based on the fact that there are optimized bandgap energy and carrier mobility for a given type of CQDSCs, we improved our CQDSC efficiency through varying the CQD bandgap energy (dot size) and altering the CQD carrier mobility using various surface passivation ligands and different ligand exchange methods. Specifically, instead of using PbX_2/AA in solution for ligand exchange, 2 types of CQDSCs using solid state layer-by-layer exchange with tetrabutylammonium iodide (TBAI) and solution exchange with methylammonium lead iodide ($MAPbI_3$) as ligands[43] were fabricated and labeled PbS-TBAI and PbS- $MAPbI_3$, respectively. The structures of these samples are shown in Figure 1 except that PbS- PbX_2/AA is replaced by PbS-TBAI and PbS- $MAPbI_3$ for our control samples. As already reported,[43] consistent with the aforementioned efficiency optimization strategy, the dependencies of CQDSC external quantum efficiency and current density on CQD bandgap energy E_g were initially found to increase with the reduction of E_g, then decrease when E_g became smaller than a threshold value between 1.28 and 1.38 eV. Limited by the scope of the experiments, an exception was the current density dependence of PbS- PbX_2/AA, which exhibited a monotonic increase with decreasing E_g without attaining a threshold value yet. In comparison, V_{oc} exhibited a positive linear dependence on the CQD bandgap energy, and it was also exchange-ligand dependent, with PbS- PbX_2/AA and PbS-$MAPbI_3$ possessing the highest and lowest V_{oc}, respectively, at all bandgap energies. All of these experimental results are in good agreement with our theoretical model predictions (section 4.2). Although mobility measurements are not discussed here, the PbS- PbX_2/AA CQDSCs were characterized with photothermal deflection spectroscopy and found to have fewer bandtail states and higher CQD packing density compared with the controls, as well as higher uniformity characterized by grazing-incidence small-angle X-ray scattering measurements. Therefore, PbS- PbX_2/AA CQDSCs were found to have the highest PCE of all CQDSCs. Regardless of the fact that PbS- $MAPbI_3$ CQD thin films had higher carrier mobility than PbS-TBAI,[44] PbS-TBAI-based CQDSCs exhibited higher PCE values than that of PbS- $MAPbI_3$, which goes against the common sense that higher mobility corresponds to better device performance. This perceived anomaly is, however, consistent with the theoretical model of section 4.2. Ultimately, the CQDSCs were optimized with a certified efficiency of 11.28 %, a bandgap energy of 1.32 eV, and a PbS-PbX_2/AA thickness of 350 nm.

J-V characteristics were obtained using a Keithley 2400 source measuring unit under simulated AM1.5 illumination (Sciencetech class A) in a continuous nitrogen flow environment. Furthermore, the calibration for spectral mismatch was conducted using a reference solar cell (Newport). Finally, following our previously reported method,[10] LIC imaging of the CQDSCs was performed in a room-temperature nitrogen environment under 10 Hz modulation frequency.

4 | RESULTS AND DISCUSSION

4.1 | Photocurrent in CQDSCs

The photocurrent density generated with illumination at short circuit can be expressed as[45]

$$J_{ph} = q\int b_s(E)EQE(E)dE, \tag{13}$$

where $b_s(E)$ is the incident spectral photon flux and EQE is the solar cell external quantum efficiency, which depends on the material absorption coefficient, charge separation efficiency, and carrier collection ability in the device, but is independent of the incident optical spectral distribution. It should be noted that J_{ph} in Equation 13 corresponds to the maximum photocurrent density that can be collected. However, as discussed above, the assumption of a constant J_{ph} is not always true for CQDSCs. Contrary to intuition, Figure 2A demonstrates that the experimental current density J_{illu} under illumination is not equal to J_{dark} - J_{sc}; instead, the current density difference (J_{ph}, according to the S-Q equation discussed in the introduction) between J_{illu} and J_{dark} is obviously voltage dependent with a shape resembling J_{illu}. The amplified dark current density J_{dark} is shown in Figure 2B and exhibits a typical exponential J-V curve. This deviation can be attributed to the low carrier mobility in CQD and organic solar cells.[29,46] Solar cell efficiency is dominated by 3 main loss factors, namely, the nonradiative recombination at the heterojunction interfaces or thin film/contact interfaces, the inefficient collection of photogenerated excitons and charge carriers, and the parasitic absorption of the contact layers.[46] Compared with high-mobility systems such as Si solar cells, the much lower carrier hopping mobility significantly reduces the charge carrier extraction rate. As a consequence, charge carriers or excitons recombine substantially at or near the location where they are created.[46] In addition, low carrier hopping mobility causes an almost open-circuit condition within the solar cell device that occurs even at short circuit,

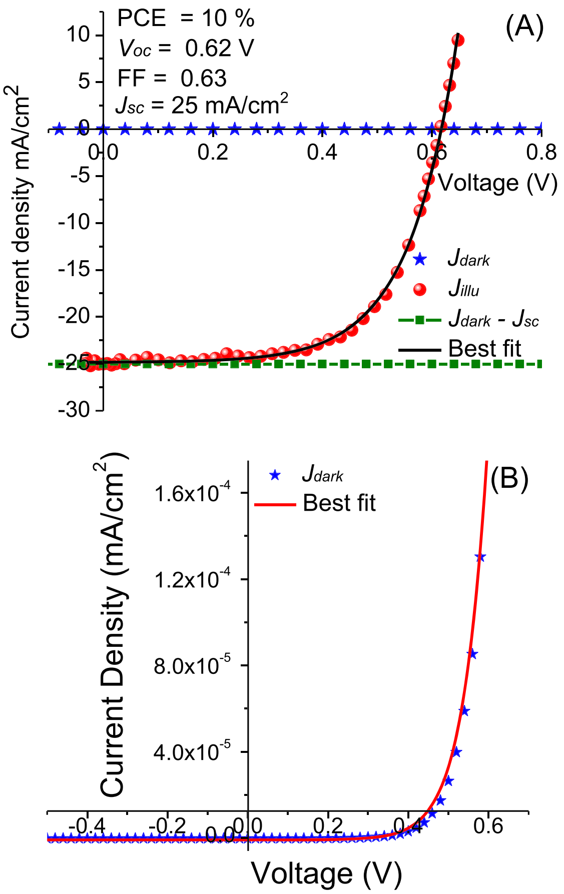

FIGURE 2 A, Experimental data and theoretical best fits of current density vs voltage under illumination and in the dark; B, the amplified dark current density J_{dark} in A. Comparison between (J_{dark} - J_{sc}) and J_{dark}, as well as J_{illu}, as a function of voltage, is also shown in A. Equations 9, 11, and 20 were used for the best fits of the J-V characteristics. The best-fitted J_{ph} at $V = 0$ (representing J_{sc}) is 24.9 mA and 7.9×10^{-7} mA under illumination and in the dark, respectively. PCE, power conversion efficiency [Colour figure can be viewed at wileyonlinelibrary.com]

leading to approximately 95% of the photogenerated carriers becoming lost to recombination as reported by Würfel et al[29] for organic solar cells with a carrier mobility equal to 10^{-6} cm^2/Vs. This phenomenon is well pronounced also in CQDSCs with increased photoactive layer thickness and/or under high illumination intensity conditions. J_{ph} is constant only when the carrier mobility is adequately high, comparable to that of commercial Si solar cells, so that the driving forces for the transport of electrons and holes can be neglected. For CQDSCs, however, carrier hopping mobility and diffusivity are very small.[6,23-28] Furthermore, the higher carrier concentration under illumination than in the dark additionally increases the conductivity of the material ($\sigma_{e,h} = e\mu_{e,h}n_{e,h}$, with $n_{e,h}$ being the carrier density of electron [e] or holes [h]) for a given hopping mobility, so the influence of driving forces for electron and hole extraction begins to emerge.[29] With this consideration in mind, we set out to develop an analytical expression for the voltage-dependent J_{ph} considering a carrier hopping drift and diffusion transport mechanism. For our solar cell sample ZnO/PbS-PbX$_2$(AA)/PbS-EDT in Figure 1, photogenerated excitons dissociate into free electrons and holes when generated in CQD layers, resulting in electric-field-dependent photocurrent with a fractional contribution, η', a function of hopping drift lengths. At voltage V_a, the mean carrier hopping drift length $\bar{L}_{drift}$ can be expressed as

$$\bar{L}_{drift} = (\mu_h\tau_h + \mu_e\tau_e)\frac{(V_{bi}-V_a)}{d}. \tag{14}$$

Therefore, the fraction η' can be extracted as the ratio of $\bar{L}_{drift}$ to the total carrier hopping drift transport length (the CQDSC thickness), ie,

$$\eta' = \frac{\bar{L}_{drift}}{L_{CQD} + L_{ZnO}}. \tag{15}$$

According to the well-known Shockley-Queisser equation, J_{ph} reverses the direction of J_{dark}, which is the net current density comprising drift and diffusion current densities and has a direction same as that of a diffusion current density under forward bias. Therefore, the direction of the built-in electric field (E_i) under equilibrium conditions is the positive direction of the photocurrent. Based on the assumption that photocarriers will be fully extracted if their hopping drift length is larger than the solar cell thickness, a case also addressed in Liu et al[43] and Gaur and Kumar,[47] the hopping drift photocurrent density can be obtained through

$$J_{ph,drift} = \begin{cases} J'_{ph}\times\eta', & when -1<\eta'<1 \\ J'_{ph}, & when\ \eta'\geq 1 \\ -J'_{ph}, & when\ \eta'\leq -1 \end{cases} \tag{16}$$

where J'_{ph} is the maximum hopping drift photocurrent density that is constant at a given illumination condition and is independent of the external voltage. Furthermore, CQD solar cell efficiencies deteriorated due to carrier transport toward wrong electrodes. Therefore, researchers have tried to add additional energy barriers, for example, the extra PbS-EDT CQD layer in Figure 1B was deposited to prevent electron diffusion to the Au electrode.[2,43] Although the influence of carrier diffusion induced carrier loss is not significant in our CQD solar cells because of the extra energy barrier introduced by PbS-EDT, for most other CQD solar cell architectures these effects are substantial and better understanding is required. Hence, in comparison with electric field induced $J_{ph,drift}$, the diffusion-associated photocurrent $J_{ph,diff}$ is also studied and found to be constant across the entire external voltage range. Specifically, hole diffusion to the ZnO is negligible due to the built-in energy barrier, while there are no (or there are much smaller) energy barriers for electron diffusion in the CQD layer. Thus, the mean diffusion distance is given by

$$\bar{L}_{diff} = \sqrt{D_e\tau_e} \tag{17}$$

and

$$\eta'' = \frac{\bar{L}_{diff}}{L_{CQD}}. \tag{18}$$

Analogous to the derivation of hoping drift photocurrent density in Equation 16, the hopping diffusion photocurrent density can be given by

$$J_{ph,diff} = \begin{cases} -J''_{ph}, & \text{when } \overline{L}_{diff} \geq L_{CQD} \\ -J''_{ph} \times \eta'', & \text{when } \overline{L}_{diff} < L_{CQD} \end{cases}. \quad (19)$$

Similarly, J''_{ph} is the maximum diffusion photocurrent density. Equation 19 reveals the negative hopping diffusion photocurrent, implying that $J_{ph,diff}$ will decrease the active total photocurrent. The negative $J_{ph,diff}$ is due to that carrier transport in a wrong direction toward the incorrect electrodes, which offsets the drift photocurrent as shown in Figure 3A,B. Therefore, the total photocurrent density J_{ph} can be obtained from adding $J_{ph,drift}$ and $J_{ph,diff}$. Figure 3A shows the dependence of J_{ph} on the external voltage using Equation 16 considering only $J_{ph,drift}$, while Figure 3B is simulated using Equations 16 and 19 with the addition of $J_{ph,diff}$, which leads to lower J_{ph} at the same mobility when compared with Figure 3A. It should be noted that J'_{ph} and J''_{ph} equal 35mA/cm^2 for the simulation in Figure 3A,B. Using the parameter values in Table 1, J_{ph} decreases with voltage except at high carrier mobilities (1 cm^2/Vs or higher) where constant J_{ph} values across the entire voltage range are obtained as shown in Figure 3A,B. Under reverse bias in Figure 3A, the external applied electric field has the same direction as E_i, thereby helping to extract charge carriers and increase J_{ph} until it saturates to the maximum $J'_{ph}-J''_{ph}$. Therefore, high reverse voltage assists the extraction of charge carriers, contributing to the overall J_{ph}.[29] This is consistent with the saturated J_{dark}-J_{illu} under reverse bias as shown in Figure 2B. The experimental J_{dark}-J_{illu} in Figure 2A is found to reduce under a forward bias, a behavior demonstrated by the simulated results in Figure 3A,B. The reduction in J_{ph} in Figure 3A is expected, as the net electric filed E_{net} reduces with increasing V_a. The resultant negative J_{ph} results from insufficient drift photocurrent to offset the negative hopping diffusion photocurrent density, which is mirrored by the negative J_{dark}-J_{illu} values when the forward voltage is larger than V_{oc}. Therefore, some special situations can be expected to arise for extremely small mobilities, such as negative J_{ph} for a mobility of 0.001 cm^2/Vs (which should be much smaller for actual CQD solar cells) in the entire V_a range when the mobility is very small or the diffusion photocurrent is sufficiently high. However, because of the restrictive assumptions as discussed below behind Equations 16 and 19 and the carrier transport parameter values used for this simulation, the negative J_{ph} for the mobility of 0.001 cm^2/Vs in Figure 3B does not mean that CQD solar cells with such a low mobility cannot materialize. In other words, J_{ph} at 0.001 cm^2/Vs can be simulated to be positive simply by adjusting the simulation parameters, for example, considering a much smaller J''_{ph} in Equation 19 or $J''_{ph} = 0$ as shown in Figure 3A. A very small J''_{ph} is true for our CQD solar cells as indicated by Figure 1B due to the energy barriers introduced by the PbS-EDT CQD layer. Figure 3A,B also show that all J_{ph} curves converge at a voltage corresponding to the intrinsic voltage V_{bi} used in Equation 14. Furthermore, lower carrier hopping mobilities μ^* lead to a lower voltage at which J_{ph} starts to drop due to a lower carrier hopping drift extraction efficiency (ie, the reduced drift length) resulting from the reduced net electrical field strength; in other words, lower mobility requires higher net electric field to extract the photocarriers. These simulated results validate the fact that when carrier hopping mobility is low, the driving forces (electric field and

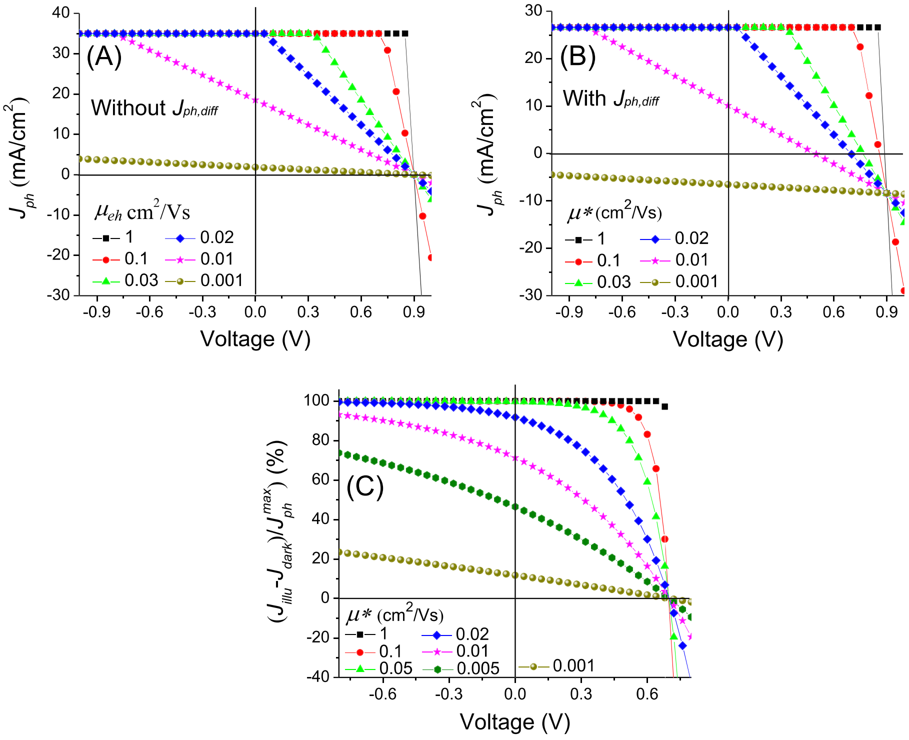

FIGURE 3 Simulated photocurrent density J_{ph} A, using Equation 16 without $J_{ph,diff}$, and B, using Equations 16 and 19 with $J_{ph,diff}$ at various effective carrier hopping mobilities; and C, $(J_{illu}-J_{dark})/J_{ph}^{max}$ as a function of the external voltage at various effective mobilities using Equation 20 [Colour figure can be viewed at wileyonlinelibrary.com]

TABLE 1 Parameters used for the colloidal quantum dot solar cell simulation

Parameter	Symbol	Value	Unit	Reference(s)
Carrier concentration at $x = 0$ at equilibrium	$n(0)$	1×10^{16}	cm^{-3}	Liu et al,[3] Kholmicheva et al,[48] and Chuang et al[49]
Solar cell thickness	d	4.1×10^{-5}	cm	Liu et al[43]
Effective hopping diffusion length	L^*	350	nm	Liu et al[43] and Sun et al[50]
Effective carrier hopping diffusivity	D^*	Varied, 1×10^{-4}-0.01	cm^2/s	Hu et al[44] and Kholmicheva et al[48]
Effective carrier hopping mobility	μ^*	Varied, 1×10^{-3}-10, 0.023 for our CQDs	cm^2/Vs	Liu et al[3,51] and Voznyy et al[52]
Built-in voltage	V_{bi}	Varied, 0.1-1.5	V	
Surface recombination velocity	S	1×10^{-3}	cm/s	Estimated from fitting
CQD bandgap energy	E_g	Varied, 0.5-3.6	eV	

diffusion gradient) for carrier transport start to impact J_{ph}. However, the experimental J-V characteristics in Figure 2A illustrate that the difference between J_{dark} and J_{illu} exhibits a nonlinear (exponential-like) dependence on the applied voltage, contrary to the linear dependence shown in Figure 3A,B using Equations 16 and 19. According to the hopping drift-diffusion J-V model, J_{ph} can be obtained through solving Equation 2 by implementing a voltage- and position-dependent carrier generation rate. For instance, the photocurrent density J_{ph} at $x = 0$ can be obtained when $J_{ph}(0) = -S(0)[n_{PV}(0) - n(0)]$ that yields an exponential dependence of J_{ph} on the applied voltage. Furthermore, free electrons and holes dissociated from photogenerated excitons generated in CQD layers contribute to electric-field-dependent and diffusion-related photocurrents with fractional contribution η' and η'', respectively, as discussed above. However, the diffusion photocurrent has been reported with negligible influence by Schilinsky et al,[53] especially for our CQD solar cells with the additional PbS-EDT layer as shown in Figure 1B. Therefore, considering the drift photocurrent extraction efficiency and that the CQD layers are the main carrier transport medium, an empirical ad hoc exponential dependence of photocurrent density on the applied voltage to represent the aforementioned hopping drift-related photocurrent densities in Equation 16 is given according to Würfel et al[29] and Gaur and Kumar[47]:

$$J_{ph} = J_{ph}^{max}\left[1 - \exp\left(\frac{(V_a - V_{bi})\mu^*\tau^*}{d^2}\right)\right], \tag{20}$$

where J_{ph}^{max} is the maximum photocurrent density that can be extracted at a given illumination level from Equation 13. For the sake of simplification, electrons and holes are considered to have the same transport parameters as defined by $\tau^* = \tau_e = \tau_h$, $L^* = L_e = L_h$, $D^* = D_e = D_h$, and $\mu^* = \mu_e = \mu_h$. Figure 3C shows the ratio $(J_{illu} - J_{dark}) / J_{ph}^{max}$ as a function of V_a using Equation 20, in agreement with the results reported for organic solar cells using a semiconductor device simulation tool TCAD Sentaurus from Synopsys Inc.[29] Furthermore, the excellent fitting of the experimental J-V characteristics in Figure 2 to the empirical expression of Equation 20 corroborates the validity of the ad hoc hopping drift-diffusion model proposed under the assumption of nonlinear exponential dependence of J_{ph} on V_a. For a high carrier hopping mobility such as 1 cm^2/Vs, all photogenerated carriers can be extracted, resulting in a typical inorganic solar cell behavior with a constant J_{ph} across the entire voltage range of interest except for the case when the external voltage becomes larger than the built-in voltage, V_{bi}, Figure 1B, and the photocurrent density drops to 0 mA/cm^2. Similar to Figures 3A,B under linear photocurrent density, the photocurrent changes direction if the external voltage increases beyond the value of the built-in potential as shown in Figure 3C. It should be noted that due to low hopping mobilities, sometimes dark and illuminated J-V curves cross, for example, the crossover point of J_{dark} and J_{illu} in Figure 2A, because of the higher carrier-population-induced higher conductivity upon illumination.[29] This effect, however, is not important in materials and devices with high carrier hopping mobilities.

4.2 | Impact of carrier hopping mobility and bandgap energy

Using the parameter values in Table 1, Figure 4A exhibits the simulated solar cell J-V characteristics and their dependence on the carrier hopping mobility ranging from 0.001 cm^2/Vs to 10 cm^2/Vs. For the sake of better comparison with our experimental CQD solar cells, the bandgap used for simulation is 1.32 eV, same as our experimentally optimized CQD energy bandgap. The mobility of CQD thin films used in our CQD solar cells has been measured to be ca. 2×10^{-2} cm^2/Vs,[51] which is also in agreement with the experimental results reported by Yazdani et al[54] for CQDs. As shown in Figure 4B, the simulated V_{oc} and J_{sc} precisely match with those measured from our CQD solar cell in Figure 2A. Furthermore, with the increase in mobility, Figure 4B, V_{oc} decreases while J_{sc} increases then saturates at high effective mobilities μ^*. The reduced V_{oc} with carrier mobility μ^* has been intensively investigated for organic solar cells, however, such studies are insufficient for CQD solar cells. Wang et al[55] and Shieh et al[56] attributed the V_{oc} loss to enhanced recombination with dark charge carriers injected from contacts at high mobilities. While it also occurs in our model, the fast extraction of charge carriers at high μ^* is another reason for low V_{oc} as predicted by Mandoc et al[57] and Deibel et al.[58] Furthermore, Tress et al[59] successfully simulated this trend of V_{oc} decline with mobility through various recombination mechanisms including Langevin recombination, recombination via charge transfer states, and trap-assisted recombination. The essential principle is the interplay between the high-mobility-boosted carrier extraction from high drift current and the enhanced carrier loss resulting from increased carrier recombination rates at high carrier mobilities. Along with the electron-hole recombination through Equations 21-23, the developed drift-diffusion current-voltage model operates as a self-consistent system considering the carrier concentration, surface recombination, and carrier

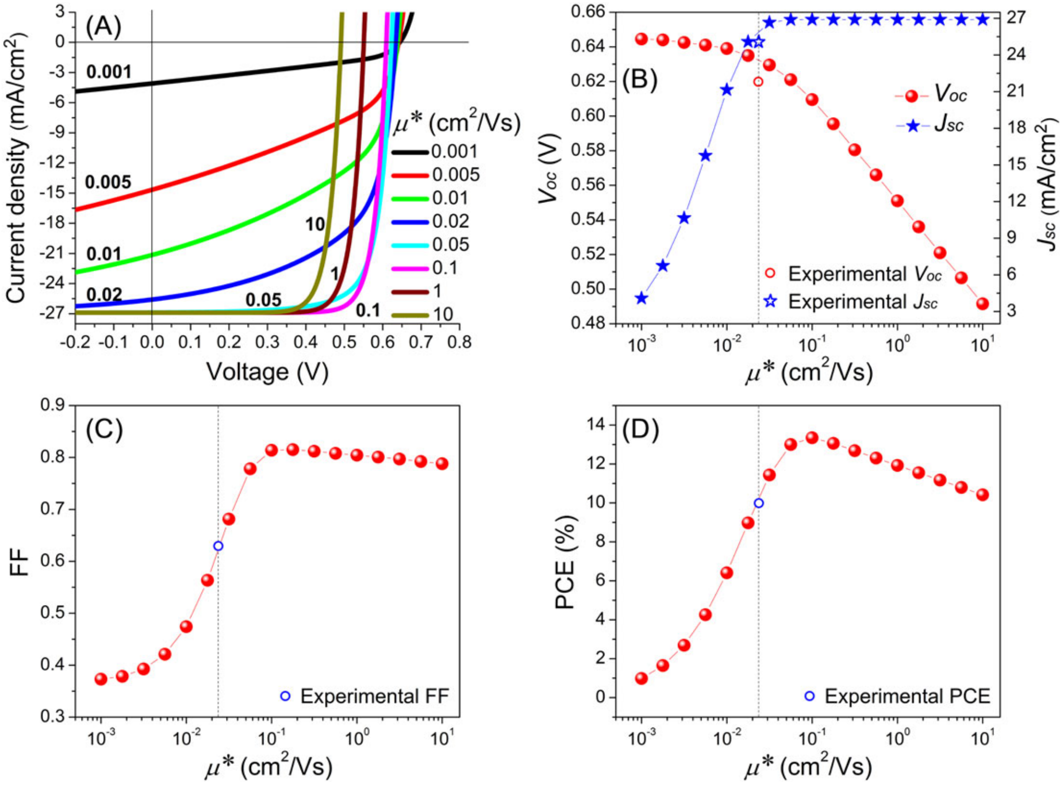

FIGURE 4 A, Simulated carrier-mobility-dependent J-V characteristics; B, open-circuit voltage V_{oc}, and short-circuit current density J_{sc}; C, fill factor FF; and D, power conversion efficiency (PCE). The colloidal quantum dot (CQD) thin film bandgap used was 1.32 eV same as our experimentally optimized bandgap for the CQD solar cell in Figure 2. The CQD solar cell carrier hopping mobility was estimated from our previous study.[51] Equations 9, 11 and 20 were used for the simulations [Colour figure can be viewed at wileyonlinelibrary.com]

hopping mobility to interpret the dependence of V_{oc}, J_{sc}, FF, and PCE on mobility. Specifically, V_{oc} is carrier concentration dependent and is determined by the energy difference between the electron and hole quasi-Fermi levels.[60] At low carrier hopping mobilities, low recombination rates yield high carrier concentrations at open circuit according to

$$eV_{oc} = \Delta E_F = kTln\left(\frac{np}{n_i^2}\right), \tag{21}$$

in which n, p, and n_i are the electron, hole, and intrinsic carrier concentrations, respectively. Furthermore, within the framework of direct electron-hole recombination, the recombination is given by

$$R_0 = \beta\left(np - n_i^2\right), \tag{22}$$

where β is the recombination constant. Langevin theory gives a description connecting the carrier mobility with recombination rate through $\beta = \frac{e(\mu_e+\mu_h)}{\epsilon_0\epsilon_r}$ with $\epsilon_0\epsilon_r$ the permittivity of the materials[61] and $\epsilon_r \approx 20$ for our CQD thin films.[3] Therefore, Tress et al[59] derived the open-circuit voltage V_{oc} as a function of mobility through β,

$$V_{oc} = \frac{1}{e}\left[E_g - k_B Tln\left(\frac{\beta N_c N_V}{G}\right)\right], \tag{23}$$

in which N_c and N_V are effective density of states on the order of 10^{19} cm^{-3} for CQDs[3] in conduction and valence bands, respectively. The term G is a carrier generation rate that equals ca. 1×10^{22} cm^{-3}s^{-1} from Tress et al.[59] Therefore, V_{oc} decreases from 0.64V to 0.49V with increasing carrier hopping mobility from 0.001 to 10 cm^2/Vs as simulated in Figure 4A,B. Taking 0.023 cm^2/Vs as our solar cell's mobility, the simulated V_{oc} is found to be close to the experimental value of 0.63V. Although current CQD fabrication techniques cannot enable mobilities in a wide range, in agreement with Figure 4B for CQD solar cells, our previous study[18] found that V_{oc} was reduced at higher temperatures that corresponds to higher carrier mobility due to the nature of phonon-assisted carrier hopping transport in these materials.[12,62] Similar simulation results for V_{oc} have also been reported for other low-mobility solar cell systems[41,58,59] using an implicit solar cell simulator. As estimated from fitting in Figure 2A, the SRV used for Figure 4 is 1×10^{-3} cm/s through Equation 11. However, when an infinite SRV is used, ie, Equation 8 with a quenching boundary condition indicating immediately recombination of all carriers arriving at the contact, V_{oc} decreases much more dramatically at high mobilities, and this effect was demonstrated in Mandoc et al[57] and Deibel et al[58] for organic solar cells. However, Deibel et al[58] found that a dramatic reduction of V_{oc} can be avoided if a finite surface recombination rate is considered. Infinite SRV is not reasonable, of course, as discussed in Wang et al,[55] also considering the significantly improved CQD surface quality of our CQD solar cells through solution-ligand exchanges that leave few unsatisfied dangling bonds on the CQD surface.[43] Furthermore, also from Figure 4B, V_{oc} is directly proportional to the bandgap energy E_g of the active photovoltaic CQD thin films, while the simulated eV_{oc} values are almost half the corresponding E_g, in agreement with the experimentally reported results for CQDSCs,[19,63] indicating that only half of the photon energy is harvested. This is due to the energy loss of excitons and charge carriers to bandgap trap states and/or bandtail states.[43] The enhanced carrier collection efficiency of the photogenerated current at higher carrier hopping mobility facilitates the increase of short-circuit current density. Short-circuit current density was obtained at zero voltage using Equations 9, 11, and 20. From Figure 3, it is expected that J_{sc} rises with mobility due to the enhanced drift photocurrent density resulting from increased mobility according to Equations 14 to 16. Theoretically, based on our model, photocurrent saturation at high mobilities occurs because all photoexcited carriers are extracted at short circuit as shown in Figure 4B, mirrored by the maximum J_{ph} values at 0 V for the high mobilities in Figure 3. In practice, further enhancement of J_{sc} can be achieved through enhancing photoexcitation intensity or absorption with small bandgap CQDs or thicker CQD layers.

Furthermore, the trade-off between J_{sc} and V_{oc} results in peaked FF and PCE with respect to carrier hopping mobilities, Figures 4C,D. The simulated FF of 0.62 at ca. 0.023 cm^2/Vs in Figure 4C is in agreement with the value of 0.63 estimated in our CQD solar cells characterized in Figure 2A. Fill factor is a measure of the current-voltage characteristic shape of solar cells. Compared with other parameters, FF can markedly elucidate carrier recombination strength.[64] Before reaching the optimized mobility as shown in Figure 4C, FF improves dramatically from the significantly enhanced carrier drift current and the marginally decreased V_{oc} as discussed above. The steep rise of FF in the low mobility regime is attributed to the increased charge carrier extraction outside the device with mobility increase while carrier recombination still remains at a relatively low level as per the drift-diffusion *J*-*V* model and Figure 4B. After attaining, the optimal carrier mobility, the decline in FF is indication that carrier recombination starts to overtake extraction. As for Figs. 4C,D, similar results of mobility-dependent FF as well as PCE are also found in low mobility organic solar cells.[59] Consequently, the study of the competition between carrier extraction and recombination, as well as the tradeoff between V_{oc} and J_{sc} with mobility, is helpful for CQD solar cell fabrication. Additionally, the simulated PCE of 9.3 % is comparable to the experimental result of 10 % shown in Figure 2A. Through literature review, despite the fact that relatively high field-effect[65-67] and terahertz radiation[68,69] mobilities have been reported on the order of 1-30 cm^2/Vs for CQDs, the highest reported solar cell PCE to date was achieved by using active materials with relative lower field-effect mobilities in a range from 10^{-3} to 10^{-2} cm^2/Vs.[23,70,71] Similar to our model, Zhitomirsky et al[21] attributed this to trap-state-limited carrier diffusion lengths; in other words, the low PCE values in higher carrier mobility materials and devices are results of increased trap-state-assisted recombination. Before the maximum PCE is attained, increasing the carrier mobility improves the PCE; however, beyond this regime, increasing the hopping mobility simply enables a higher rate of carrier recombination. Therefore, instead of intuitively pursuing higher carrier mobility, a more effective suggestion for solar cell performance optimization should be to reduce the trap state which also reduce bimolecular recombination due to strengthened interdot coupling and enhance the diffusion length, then to further increase carrier mobility. In conclusion, the simulated results in Figure 4 are in agreement with the finding that "low mobility might help mitigate a particular loss mechanism in a certain material ..." as reported by Street et al.[61]

Colloidal quantum dots are promising in solar cell fabrication due to their dot-size-tunable bandgap energy, thereby making the structural design for harvesting more solar energy much easier. A simulation of CQD bandgap-energy-dependent PCE, Figure 5, was conducted using Equation 13, for the sake of simplification, with an approximated average *EQE* = 0.76 when the incident light energy is higher than the CQD thin film bandgap energy according to our fitting shown in Figure 2; otherwise, *EQE* = 0. However, more precise experimental

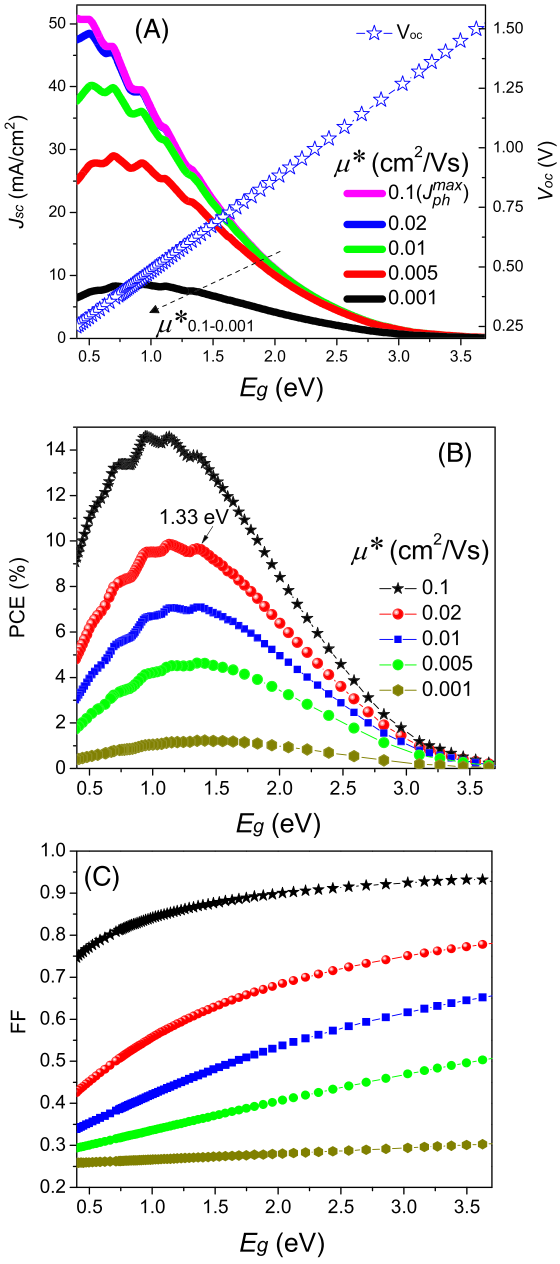

FIGURE 5 Theoretical simulations of colloidal quantum dot solar cell electrical parameters: A, V_{oc} and J_{sc}; B, power conversion efficiency; and C, FF as functions of colloidal quantum dot bandgap energy (E_g) for 5 different carrier hopping mobilities. The maximum photocurrent J_{ph}^{max} is the same as J_{sc} at the mobility of 0.1 cm^2/Vs. The illumination intensity used for the simulation is AM1.5 spectrum at 1 sun intensity. Equations 9, 11, 20, and 24 were used for the simulations [Colour figure can be viewed at wileyonlinelibrary.com]

EQE values as a function of wavelength can be found in Liu et al[43] for further research investigations. Therefore, considering AM1.5 excitation, J_{ph}^{max} was obtained by integrating the product of *EQE*, $b_s(E)$, and the photon energy according to Equation 13. Subsequently, J_{sc} was calculated by combining Equations 9, 11, 13, and 20 at 0V external voltage. Smaller E_g facilitates absorption of photons with lower energy, leading to an increased maximum photocurrent density J_{ph}^{max}, Figure 5A. However, because of the hopping mobility-dependent J_{sc}, which equals J_{ph} at short circuit, J_{ph}^{max} converges to J_{sc} only at 0.1 cm^2/Vs across the whole simulated E_g range. The slight drop in J_{sc} at small E_g for all mobilities is due to the scarcity of significant low-wavelength solar energy according to the nature of the AM1.5 solar spectrum, ie, J_{ph}^{max} starts to saturate as shown in Figure 5A. In addition, it is also due to the decreased built−in voltage V_{bi} (corresponding to lowered V_{oc}) that is reduced when the CQD photovoltaic material E_g decreases according to Equation 20. Therefore, compared with higher mobilities, J_{sc} is expected to start to decrease at higher E_g for low carrier mobilities as shown in Figure 5A. A linear dependence of V_{oc} on E_g was found and extracted by linear best fits of the experimental data[43] from our CQDSCs, Figure 5A, and it could be expressed as

$$V_{oc} = 0.387E_g + 0.095. \tag{24}$$

Here, the units of V_{oc} and E_g are V and eV, respectively. A similar linear dependence of V_{oc} on E_g has also been reported by Bozyigit et al[19] in the form of $0.27E_g + 0.09$ for ligand EDT capped PbS CQDSCs. Insofar as the trade-off between J_{sc} and V_{oc}, an optimized CQD bandgap energy for a maximized PCE value can be expected. In other words, although small-bandgap CQDs facilitate solar energy absorption in a wider wavelength range, the reduced E_g compromises V_{oc} according to Equations 23 and 24. The simulated PCE in Figure 5B is through Equations 9, 11, 13, 20, and 24 and the calculated J_{sc} and V_{oc} as discussed above. Therefore, applying the given carrier hopping transport parameters as tabulated in Table 1, the simulation of PCE in Figure 5B yields an optimized E_g of ~1.12 eV for a mobility of 0.02 cm^2/Vs, a mobility estimated for our CQD systems.[51] Because of the nature of AM1.5 spectrum, multiple PCE subpeaks are also observed, a feature consistent with the J_{sc} in Figure 5A and the well-known Shockley-Queisser limit simulation. As discussed in Section 3, the experimentally optimized E_g is 1.32 eV, which is close to the subpeak labeled in Figure 5B. It should be noted that, experimentally, only CQD bandgap values in a range between 1.28 to 1.48 eV were tried.[43] The PCE simulation implies there is still room for further PCE improvement using CQD materials at this mobility. The bandgap-dependent PCEs for other mobilities in Figure 5B reveal a blue-shift of the optimized E_g with mobility increase, which is in agreement with Würfel et al.[29] The shift to small bandgap is a result of relatively high carrier drift current at high mobilities. Specifically, the reduced E_g diminishes the intrinsic electric field and the drift current starts to decrease at smaller E_g for higher carrier mobilities when compared with lower-mobility CQD solar cells. This overall nonmonotonic

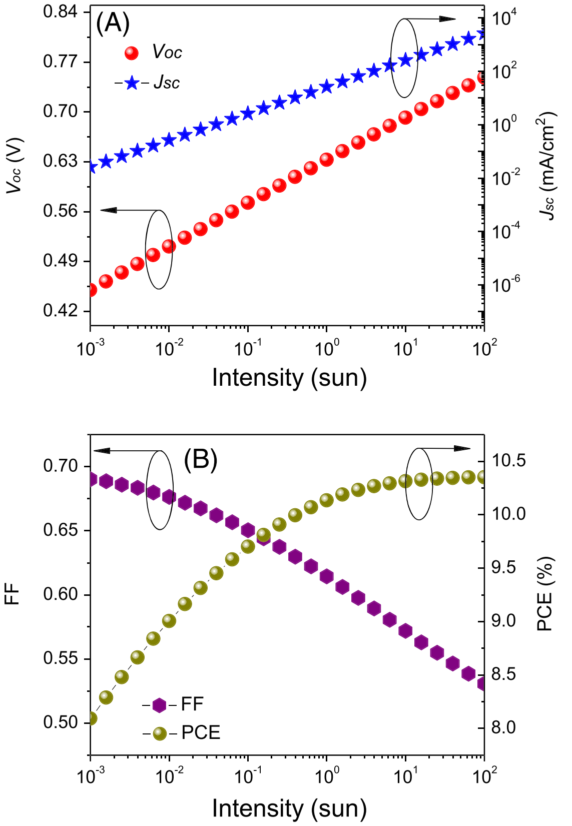

FIGURE 6 A, Simulated colloidal quantum dot solar cell V_{oc} and J_{sc}, as well as B, FF and power conversion efficiency (PCE), as functions of the illumination intensity. Equations 9, 11, and 20 were used for the simulations [Colour figure can be viewed at wileyonlinelibrary.com]

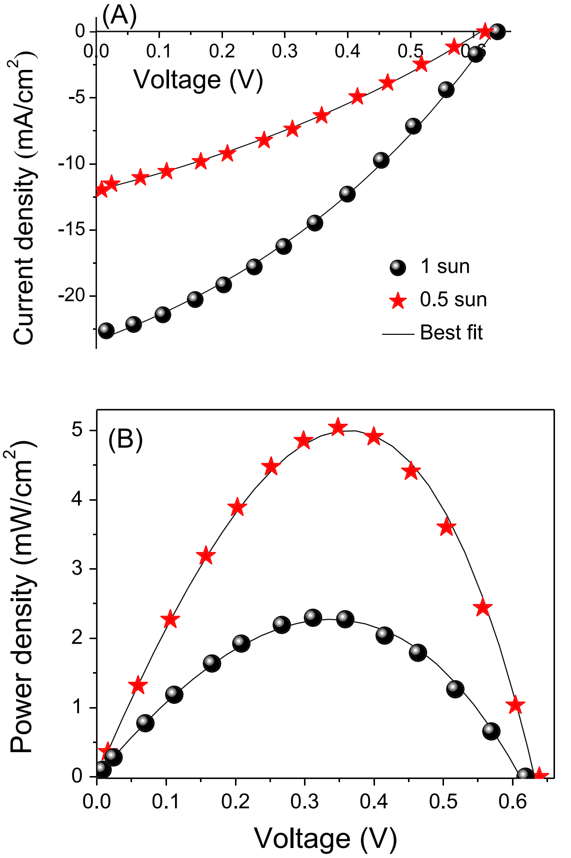

FIGURE 7 A, Experimental J-V characteristics and B, colloidal quantum dot solar cell output power as a function of photovoltage. Continuous lines are best fits to the J-V characteristics and output powers using Equations 9, 11, and 20 [Colour figure can be viewed at wileyonlinelibrary.com]

behavior in Figure 5A implies an increased PCE with the simulated carrier hopping mobility in a range where the carrier extraction rate still surpasses the recombination rate. Furthermore, possible simulation deviation of this model is expected due to the use of linear E_g-dependent V_{oc} through Equation 24, which, however, is derived based on experimental data in a narrow E_g range, probably not sufficiently accurate for a wide-range E_g simulation in this study. In addition, for small E_g with high photoexcited carrier densities V_{oc} should be further reduced, as there will be an exponential dependence of V_{oc} on carrier concentration according to Equations 21 and 23. The latter will lead to even lower V_{oc} at smaller E_g than Equation 24 predicts, resulting in a shift of the optimized E_g to large E_g CQDs. Figure 5C shows a monotonic increase of FF with E_a as well as with μ^* in the range between 0.001 and 0.1 cm^2/V. As discussed above, the increased FF values indicate that with increased bandgap, carrier extraction plays an increasingly important role in carrier transport over recombination processes according to Figure 5C.

The foregoing hopping drift-diffusion J-V model was further examined by studying the effects of illumination intensity on the solar cell V_{oc}, J_{sc}, FF, and PCE. Figure 6A validates the enhanced J_{sc} with illumination intensity due to boosted photoexcited carrier densities. The simulated V_{oc} shows an exponential correlation with the excitation intensity as shown in Figure 6A that is mirrored in the well-known relation $V_{oc} = A + \frac{n_{id}kT}{q} lnX$, in which A is a constant and X represents the illumination intensity. According to recombination mechanisms including the Langevin and trap-state-assisted Schockley-Read-Hall (SRH) recombination theories, the carrier recombination rate changes proportional to the carrier concentration. For example, through direct bimolecular recombination, Equation 22, the carrier recombination rate grows with carrier concentration proportional to the photoexcitation intensity. With carrier recombination increase, Figure 6B shows decreasing FF at high excitation intensities, in good agreement with the experimental findings reported by Wang[72] and Proctor et al.[73] Because of the increased carrier recombination rate at high photocarrier injection levels, PCE increases only slightly from approximately 8.0% at 0.001 sun to approximately 10.1% at 1 sun illumination in agreement with our CQD solar cells in Figure 2A, above which the PCE increase slows down and even saturates at high illumination intensities. This implies that with the consideration of various carrier recombination pathways, carrier radiative and nonradiative recombinations through different mechanisms such as direct biomolecular or SRH approaches can degrade CQD solar cell performance significantly at high mobilities and/or high photocarrier injection levels. However, one should be aware that at sufficiently high mobilities comparable to conventional Si solar cells, this model should not be applied as the effects of electric and diffusion forces become trivial and negligible. Approaches to reduce carrier recombination in CQD systems can be through reducing exciton binding energy and/or through removing material trap states.

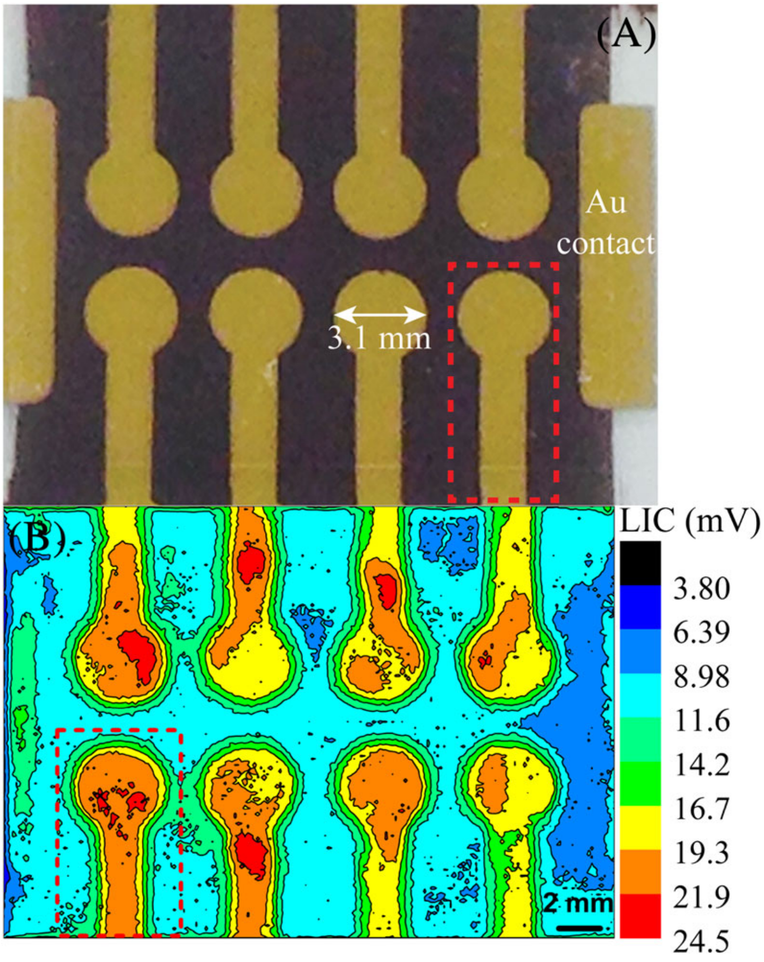

FIGURE 8 A, A photograph of a colloidal quantum dot solar cell sample and B, its lock-in carrierography (LIC) image at open circuit after the cell was flipped over with the Au contacts on the bottom. The excitation laser was frequency-modulated at 10 Hz at a mean intensity of 1 sun. The 8 Au-coated thin-film electrodes on the top in A are electrical contacts while dark brown regions are without Au contact layers. Both regions have an energy structure as shown in Figure 1B. The Au electrode circumscribed with a dashed rectangle in A and also shown in the flipped over orientation in B is further studied in Figures 9 and 10 [Colour figure can be viewed at wileyonlinelibrary.com]

High exciton binding energy facilitates the probability for electrons and holes to recombine.[52] An effective approach is to dissociate excitons through strengthening interdot coupling and/or increase interface energy barriers through a heterojunction architecture. Strong interdot coupling can be realized with the use of high-quality and monodispersed CQDs that remove defects and trap states in CQDs. Therefore, improving CQD quality through various methods as discussed in the introduction always contributes to improved CQD solar cell performance.

4.3 | Impact of electrode-semiconductor interface using LIC imaging

Equation 10, a boundary condition in the hopping drift-diffusion model above, reveals the dependence of CQDSC J-V characteristics on surface recombination velocity *S*(*d*), a parameter determined by the CQD thin-film surface passivation or trap states at CQD semiconductor/Au electrode interfaces, Figure 1. A better electrode coating with lower interface states leads to low *S*(*d*) that results in higher CQDSC

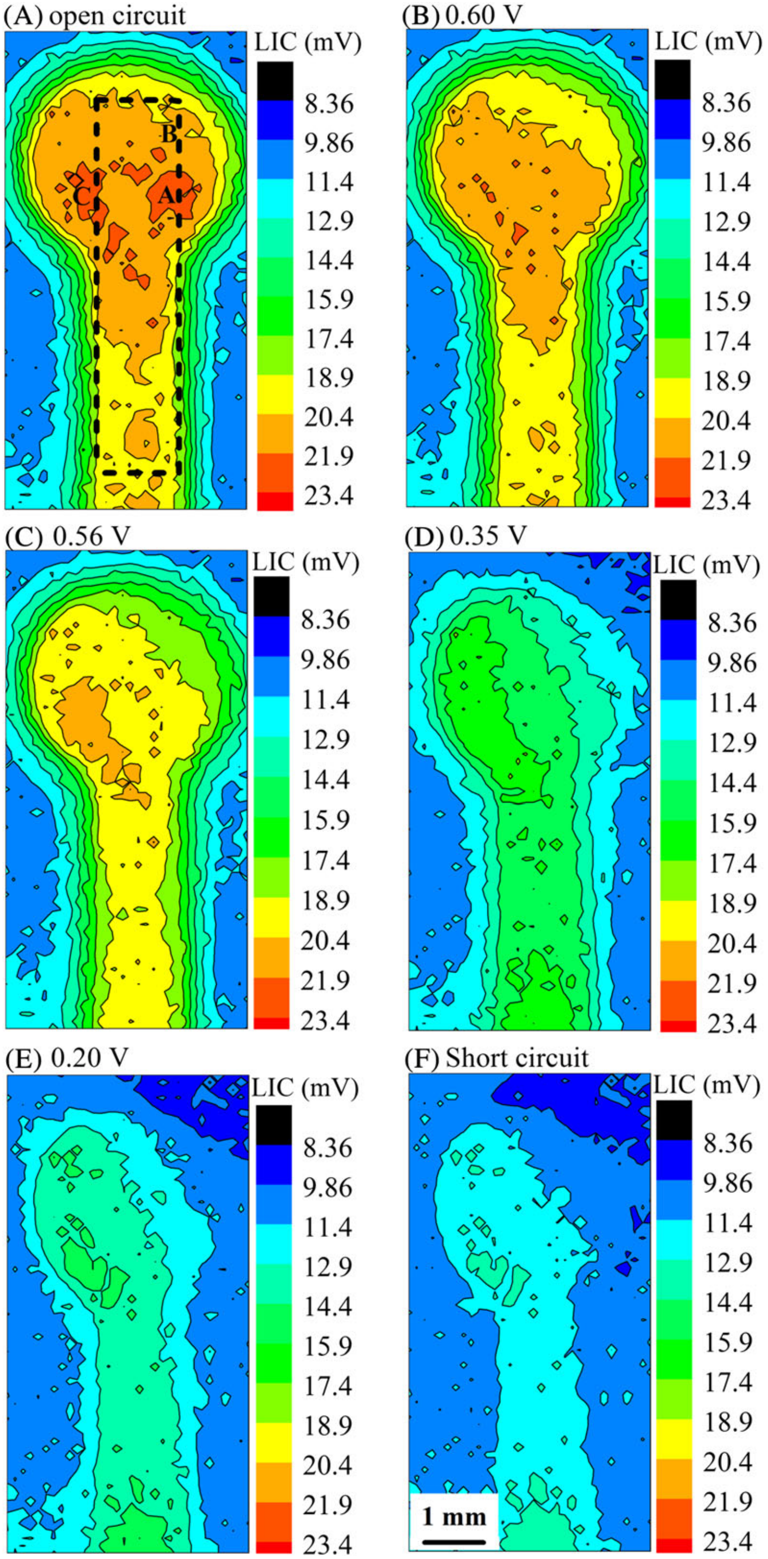

FIGURE 9 Lock-in carrierography (LIC) images of the circumscribed colloidal quantum dot solar cell Au electrode in Figure 8 at open-circuit A, 0.64 V; B, 0.60 V; C, 0.56 V; D, 0.35 V; E, 0.20 V; and F, short-circuit. The excitation laser was frequency modulated at 10 Hz at a mean intensity of 1 sun. [Colour figure can be viewed at wileyonlinelibrary.com]

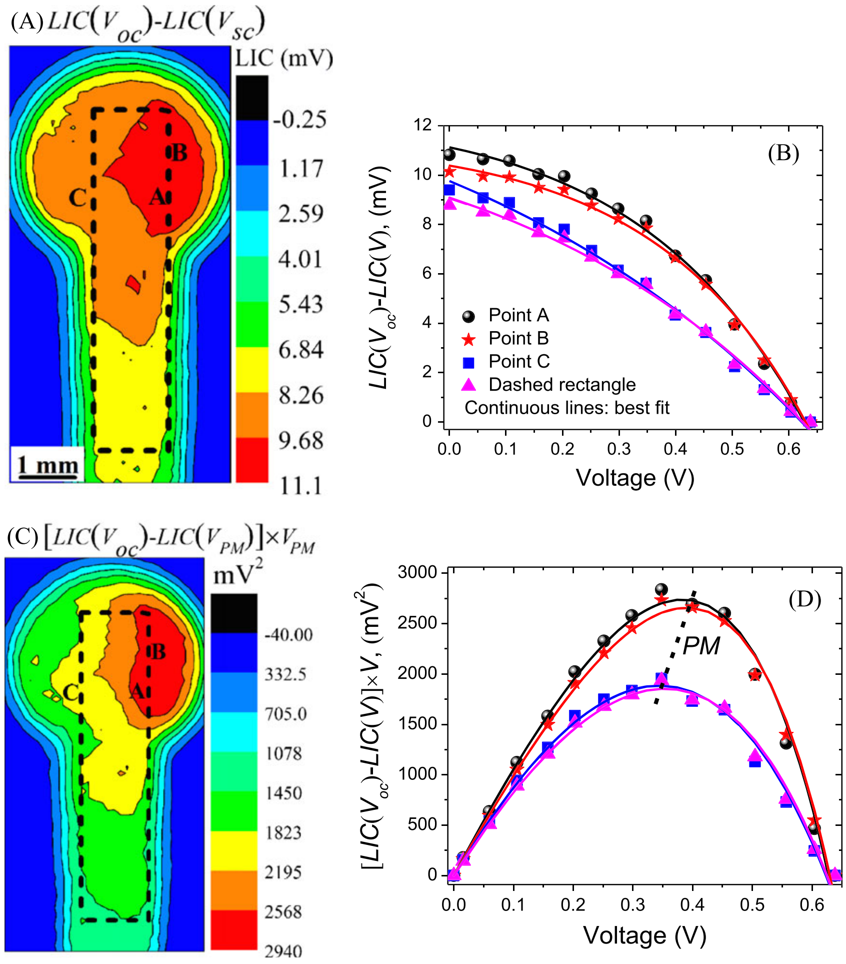

FIGURE 10 Lock-in carrierography (LIC) of the circumscribed colloidal quantum dot solar cell Au electrode in Figure 8: A, *LIC* (V_{oc}) - *LIC*(V_{sc}); B, [*LIC* (V_{oc}) - *LIC* (*V*)] vs *V*; C, [*LIC* (V_{oc}) - *LIC*(V_{PM})]V_{PM}; and D, [*LIC*(V_{oc}) -*LIC*(*V*)] *V* vs *V* characteristics. The excitation laser was frequency modulated at 10 Hz at a mean intensity of 1 sun. B and D are best fitted to Equation 25. Points A, B, C, and the dashed rectangle region are shown in A and C. It should be noted that values calculated for the dashed rectangle region are based on averaging the LIC amplitudes over all pixels in this region. Furthermore, PM denotes maximum power, ie, the maximum value of [*LIC*(V_{oc}) -*LIC*(*V*)] *V* [Colour figure can be viewed at wileyonlinelibrary.com]

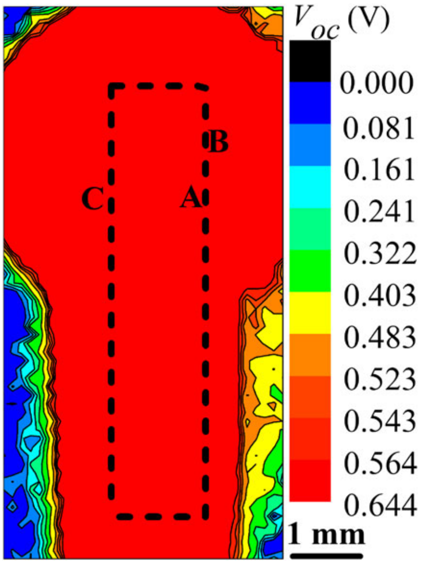

FIGURE 11 Lock-in carrierography contour mapping of the open-circuit voltage V_{oc} for the circumscribed colloidal quantum dot solar cell Au electrode in Figure 8 [Colour figure can be viewed at wileyonlinelibrary.com]

TABLE 2 Optical counterparts of colloidal quantum dot solar cell electrical parameters, obtained through best-fitting of the experimental data in Figures 10B,D to Equation 25

Sample	J_R/C_{LIC} (C·mV)	J_{R0}/C_{LIC} (C·mV)	m' (V^{-1})
Point A	1.78×10^{-18}	2.34×10^{-19}	3.43
Point B	1.66×10^{-18}	1.71×10^{-19}	3.76
Point C	1.56×10^{-18}	1.02×10^{-18}	1.49
Selected Region	1.45×10^{-18}	6.45×10^{-19}	1.89

performance. To investigate the CQD/Au interface effects on CQDSC performance, nondestructive imaging (NDI) of carrier population distributions and key photovoltaic parameters was conducted using LIC, a spectrally gated dynamic frequency-domain photoluminescence-based transport property imaging method.[10,37] The LIC images revealed the complexity and inhomogeneity of the electrode-coating-associated surface recombination in our experimental CQDSCs. As shown in Figure 7, the J-V and P-V characteristics of one solar cell with lower PCE when compared with Figure 2 exhibited similar V_{oc} values but much lower J_{sc} and were best fitted to the combination of Equations 9, 11, and 20 with the consideration of Au-electrode-modified surface recombination velocity. For excitonic transport and dissociated free carrier radiative recombination, the voltage-dependent optical carrier flux corresponding to its electrical counterpart Equation 9 was introduced by Mandelis et al[74] and subsequently used by Liu et al[75] for mc solar cells as their Equation 18; it was further adapted here with a different optoelectronic coefficient $m'\left[= \left(\frac{\mu^*}{D^*}\right)'\right]$ for hopping transport in CQDSCs:

$$J[\hbar\omega, V(\hbar\omega)]_r = J_R - J_{R0}\left[e^{m'V(\hbar\omega)} - 1\right]. \tag{25}$$

$J[\hbar\omega, V(\hbar\omega)]_r$ can also be obtained experimentally through

$$J[\hbar\omega, V(\hbar\omega)]_r = qC_{LIC}[LIC(V_{oc}) - LIC(V(\hbar\omega))], \tag{26}$$

where LIC is the lock-in carrierography signal at photovoltage $V(\hbar\omega)$, $J[\hbar\omega, V(\hbar\omega)]_r$ is the non-equilibrium radiative recombination current density, J_R and J_{R0} are the relevant current-density-like quantities, and C_{LIC} is a coefficient defined as[75]

$$C_{LIC} = \frac{|I_i|(1-R)\eta}{\hbar\omega_{in}\,[LIC(V_{oc}) - LIC(0)]}\left[\frac{1-\eta_{ce}(\hbar\omega, V=0, T)}{1-\lambda_{in}\lambda_{em}^{-1}}\right], \tag{27}$$

where $|I_i|$ is the peak value of the incident modulated illumination intensity; R is the surface reflectance; η and $\eta_{ce}(\hbar\omega, V=0, T)$ are the quantum efficiency for exciton and charge carrier photo-generation and photocarrier-to-current collection efficiency; $\hbar\omega_{in}$ is the incident photon energy; and λ_{in} and λ_{em} are, respectively, the incident and emitted photon wavelength. In a manner similar to the electrical Equations 9 and 11, Equation 25 links the exciton and free carrier radiative recombination flux, which is an optically measurable quantity to its electrical parameter counterparts. The expressions for J_{ph}, J_0, V_{oc}, and m' have been derived by Liu et al[75] using the optical parameters in Equation 25 and a photocarrier-to-current collection efficiency, which is the ratio of the photocarrier flux collected by the solar cell electrodes (giving rise to the photocurrent) to the incident photocarrier flux. A photograph of our solar cell is presented in Figure 8A, and the corresponding LIC image shown in Figure 8B reveals the inhomogeneities of the Au contact regions which are distinguishable from those without Au layers. A dashed rectangle in Figure 8A, same as the one circumscribed in Figure 8B, is circumscribed around the perimeter of an Au layer and is further studied in detail in Figures 9–11. The LIC image-generating laser was introduced from the ITO/ZnO side, Figure 1. The image contrast originates in inhomogeneous exciton and free charge carrier population distributions due to mechanical or electrical defect-induced photocarrier lifetime variations. Defect-induced trap states act as thermal capture and emission centers of a nonradiative recombination nature that diminish exciton and free charge carrier hopping lifetimes, resulting in LIC image signal decreases. According to Figure 8B, regions (solar cell pixel images) with electrodes on the right-hand side appear to have higher defect densities or worse contacts than those on the left-hand side. These observations are consistent with our experimental results that low solar cell efficiency is associated with J-V measurements of these particular solar cell units. These results show that carrier diffusion-wave-based LIC imaging has excellent potential for nondestructive inspection of CQDSCs. For solar cell PCE optimization, dynamic carrier distribution visualization as a function of applied external voltage, Figure 9, is crucial for optimizing device fabrication with respect to materials and nanoparticle deposition techniques. With decreasing external voltage, the LIC image exhibits different trends in different regions within the entire solar cell unit image, indicating highly inhomogeneous carrier hopping transport. These variations in performance of each device lead to a poor overall solar cell behavior and should be considered seriously as optimization issues for commercial CQDSC fabrication. Specifically, points A, B, C, and the area inside the dashed rectangle were studied as shown in Figure 9A. Excitons and charge carriers extracted into the external circuit through the Au and ITO contacts in Figure 1 can be probed through LIC signal differences between open-circuit and short-circuit conditions, Figures 10A,B. It can be observed from Figures 10A,C that more photogenerated excitons and free charge carriers are collected at points A and B than at point C and at regions close to the edge of the contacts. Excellent best fits to our theoretical model Equation 25 have been achieved as shown in Figures 10B,D, in addition to the best-fitted optical parameters shown in Table 2. The results reveal that high-amplitude regions in Figure 10A,C yield higher optical counterparts of J_{ph} and the optoelectronic coefficient, along with lower optical saturation current densities. A conclusion can be reached from Figure 10B that defects compromise the optical I_{sc} more significantly than V_{oc}, which remains almost constant at all 3 selected points and inside the dashed rectangle region. The LIC images thus suggest that material surface and interface treatments for eliminating CQD surface defects may benefit V_{oc} enhancement only in a limited manner although they can raise J_{sc} significantly. Therefore, smaller J_{sc} values arising from higher defect state density result in reduced maximum-output-powers P_{max} as shown in Figures 10C,D, which present the maximum-output-power mapping and its voltage dependence, respectively. In comparison, the solar cell pixel V_{oc} image, Figure 11, is more homogeneous within the Au electrode region as the Fermi level splitting determined V_{oc} is controlled primarily by the work function difference between its corresponding electrodes rather than device defects or defect-affected carrier hopping transport behavior at a given mobility as discussed in section 4.2. Figures 10 and 11 clearly demonstrate the critical importance of electrode influence on CQDSC performance. The respective maximum power and carrier collection LIC images are critical to the evaluation of the CQDSC quality due to the low carrier hopping mobility and diffusivity that result in low collection efficiency of carriers generated far away (compared to a diffusion length) from the carrier extraction electrodes.

5 | CONCLUSIONS

A comprehensive CQDSC efficiency optimization strategy with respect to CQD carrier mobility μ, bandgap energy E_g, illumination intensity, and electrode interface was proposed and implemented for the first time. Following this strategy, CQDSCs with a certified efficiency as high as 11.28 % were fabricated through screening surface passivation ligands, CQD energy bandgap energies, as well as optimized active CQD thin film thickness. The optimized μ and E_g were determined from the new analytical theoretical model introduced for maximizing the device PCE, which provided a quantitative strategy for device efficiency improvement based on physical transport processes as opposed to the empirical procedures used by most researchers to date. Furthermore, the universally applied assumption of constant photocurrent was revisited, shown to be invalid, and the variation with voltage was validated for CQDSCs. Large-area inspection of CQDSC carrier population distributions, collection efficiency, and V_{oc} using LIC imaging revealed a strong correlation between Au electrode/CQD interface associated surface recombination effects and solar cell performance. This strategy shifts the optimization methodology away from the prevailing conventional small-spot characterization methodologies and their limitations. The developed self-consistent analytical hopping drift-diffusion-wave model together with the large-area LIC NDI pave the way for a quantitative comprehensive strategy for device fabrication toward higher efficiency solar cells that can be of great interest to the CQDSC community. The presented efficiency optimization strategy is summarized below.

1. Attempts to enhance the carrier diffusion length by reducing trap state density either through selecting proper interdot linking ligands that have lower lattice mismatch with the CQD crystal lattice or through the use of solution-based ligand exchanges, rather than the solid state layer-by-layer method,[43] should always be the first priority.
2. According to the achieved diffusion length, the proper CQD thin-film thickness for solar cells should be determined, and the present new drift-diffusion transport model that introduces voltage-dependent J_{ph} should be used to find optimized μ and E_g at a maximized PCE for the given estimated parameters as shown in Table 1.
3. Only after the diffusion length improves, efforts to reduce CQD polydispersity or strengthen interdot coupling to reach an optimized μ at a given CQD E_g should be implemented guided by the parameter relationships shown in Figure 4.
4. Since μ cannot be characterized in as straightforward a manner as E_g, the preferred procedure should be to use dot-size-tunable E_g, instead of varying μ, toward achieving maximum PCE according to Figure 5.
5. Eliminating material surface and interface defects benefits V_{oc} enhancement only in a limited manner but can raise J_{sc} significantly. Therefore, selection of electrode metals and contact procedures yielding optimal carrier density distributions, extraction efficiency, and V_{oc} as visualized by LIC imaging is an effective tool for further CQDSC efficiency improvement.

ACKNOWLEDGEMENTS

The authors are grateful to the Natural Sciences and Engineering Research Council of Canada (NSERC) for a discovery grant to A.M. and to the Canada Research Chairs program.

ORCID

Lilei Hu http://orcid.org/0000-0002-8493-2440

REFERENCES

1. Best research cell efficiencies (https://www.nrel.gov/pv/assets/images/efficiency-chart.png), National Center for Photovoltaics, National Renewable Energy Laboratory (USA), Golden, CO. (accessed June 22, 2017).
2. Chuang CH, Brown PR, Bulović V, Bawendi MG. Improved performance and stability in quantum dot solar cells through band alignment engineering. *Nat Mater*. 2014;13(8):796-801.
3. Liu M, de Arquer F, Li Y, et al. Double-sided junctions enable high-performance colloidal-quantum-dot photovoltaics. *Adv Mater*. 2016;28(21):4142-4148.
4. Wang X, Koleilat GI, Tang J, et al. Tandem colloidal quantum dot solar cells employing a graded recombination layer. *Nat Photonics*. 2011;5(8):480-484.
5. Lan X, Voznyy O, Kiani A, et al. Passivation using molecular halides increases quantum dot solar cell performance. *Adv Mater*. 2016;28(2):299-304.
6. Yuan M, Kemp KW, Thon SM, et al. High-performance quantum-dot solids via elemental sulfur synthesis. *Adv Mater*. 2014;26(21):3513-3519.
7. Ning Z, Voznyy O, Pan J, et al. Air-stable n-type colloidal quantum dot solids. *Nat Mater*. 2014;13(8):822-828.
8. McDonald SA, Konstantatos G, Zhang S, et al. Solution-processed PbS quantum dot infrared photodetectors and photovoltaics. *Nat Mater*. 2005;4(2):138-142.
9. Turyanska L, Patane A, Henini M, Hennequin B, Thomas NR. Temperature dependence of the photoluminescence emission from thiol-capped PbS quantum dots. *Appl Phys Lett*. 2007;90(10):101913.
10. Hu L, Yang Z, Mandelis A, et al. Quantitative analysis of trap-state-mediated exciton transport in Perovskite-Shelled PbS quantum dot thin films using photocarrier diffusion-wave nondestructive evaluation and imaging. *J Phys Chem C*. 2016;120(26):14416-14427.
11. Tisdale WA, Williams KJ, Timp BA, Norris DJ, Aydil ES, Zhu XY. Hot-electron transfer from semiconductor nanocrystals. *Science*. 2010;328(5985):1543-1547.
12. Romero HE, Drndic M. Coulomb blockade and hopping conduction in PbSe quantum dots. *Phys Rev Lett*. 2005;95(15):156801.
13. Xu S, Thian D, Wang S, Wang Y, Prinz FB. Effects of size polydispersity on electron mobility in a two-dimensional quantum-dot superlattice. *Phys Rev B*. 2014;90(14):144202.
14. Chu IH, Radulaski M, Vukmirovic N, Cheng HP, Wang LW. Charge transport in a quantum dot supercrystal. *J Phys Chem C*. 2011;115(43):21,409-21,415.
15. Liu Y, Gibbs M, Puthussery J, et al. Dependence of carrier mobility on nanocrystal size and ligand length in PbSe nanocrystal solids. *Nano Lett*. 2010;10(5):1960-1969.
16. Kramer IJ, Sargent EH. The architecture of colloidal quantum dot solar cells: materials to devices. *Chem Rev*. 2013;114(1):863-882.
17. Hu L, Mandelis A, Melnikov A, Lan X, Hoogland S, Sargent EH. Study of Exciton hopping transport in PbS colloidal quantum dot thin films using frequency-and temperature-scanned photocarrier radiometry. *Int J Thermodyn*. 2017;38(1):7.
18. Hu L, Mandelis A, Lan X, Melnikov A, Hoogland S, Sargent EH. Imbalanced charge carrier mobility and Schottky junction induced anomalous current-voltage characteristics of excitonic PbS colloidal quantum dot solar cells. *Sol Energy Mater Sol Cells*. 2016;155:155-165.
19. Bozyigit D, Lin WM, Yazdani N, Yarema O, Wood V. A quantitative model for charge carrier transport, trapping and recombination in nanocrystal-based solar cells. *Nat Commun*. 2015;6:6180.
20. Mandelis A, Hu L, Wang J. Quantitative measurements of charge carrier hopping transport properties in depleted-heterojunction PbS colloidal quantum dot solar cells from temperature dependent current–voltage characteristics. *RSC Adv*. 2016;6(95):93180-93194.
21. Zhitomirsky D, Voznyy O, Levina L, et al. Engineering colloidal quantum dot solids within and beyond the mobility-invariant regime. *Nat Commun*. 2014;5:3803.
22. Shockley W, Queisser HJ. Detailed balance limit of efficiency of p-n junction solar cells. *J Appl Phys*. 1961;32(3):510-519.

23. Ip AH, Thon SM, Hoogland S, et al. Hybrid passivated colloidal quantum dot solids. *Nat Nanotechnol*. 2012;7(9):577-582.

24. Tang J, Brzozowski L, Barkhouse DA, et al. Quantum dot photovoltaics in the extreme quantum confinement regime: the surface-chemical origins of exceptional air-and light-stability. *ACS Nano*. 2010;4(2): 869-878.

25. Bozyigit D, Volk S, Yarema O, Wood V. Quantification of deep traps in nanocrystal solids, their electronic properties, and their influence on device behavior. *Nano Lett*. 2013;13(11):5284-5288.

26. Johnston KW, Pattantyus-Abraham AG, Clifford JP, et al. Efficient Schottky-quantum-dot photovoltaics: the roles of depletion, drift, and diffusion. *Appl Phys Lett*. 2008;92(12):122111.

27. Clifford JP, Konstantatos G, Johnston KW, Hoogland S, Levina L, Sargent EH. Fast, sensitive and spectrally tuneable colloidal-quantum-dot photodetectors. *Nat Nanotechnol*. 2009;4(1):40-44.

28. Jeong KS, Tang J, Liu H, et al. Enhanced mobility-lifetime products in PbS colloidal quantum dot photovoltaics. *ACS Nano*. 2011;6(1):89-99.

29. Würfel U, Neher D, Spies A, Albrecht S. Impact of charge transport on current-voltage characteristics and power-conversion efficiency of organic solar cells. *Nat Commun*. 2015;6:6951.

30. Hameiri Z, Mahboubi Soufiani A, Juhl MK, et al. Photoluminescence and electroluminescence imaging of perovskite solar cells. *Prog Photovolt Res Appl*. 2015;23(12):1697-1705.

31. Hinken D, Ramspeck K, Bothe K, Fischer B, Brendel R. Series resistance imaging of solar cells by voltage dependent electroluminescence. *Appl Phys Lett*. 2007;91(18):182104.

32. Ramspeck K, Bothe K, Hinken D, Fischer B, Schmidt J, Brendel R. Recombination current and series resistance imaging of solar cells by combined luminescence and lock-in thermography. *Appl Phys Lett*. 2007;90(15):153502.

33. Sun Q, Melnikov A, Mandelis A. Quantitative self-calibrating lock-in carrierographic lifetime imaging of silicon wafers. *Appl Phys Lett*. 2012;101(24):242107.

34. Sun Q, Melnikov A, Mandelis A. Camera-based high frequency heterodyne lock-in carrierographic (frequency-domain photoluminescence) imaging of crystalline silicon wafers. *Phys Status Solidi (a)*. 2016;213(2): 405-411.

35. Sun Q, Melnikov A, Mandelis A. Quantitative heterodyne lock-in carrierographic imaging of silicon wafers and solar cells. In Proceedings, 40th IEEE Photovoltaic Specialist Conference (PVSC), 2014:1860-1865.

36. Melnikov A, Chen P, Zhang Y, Mandelis A. Lock-in and heterodyne carrierographic imaging characterization of industrial multicrystalline silicon solar cells. *Int J Thermodyn*. 2012;33 (10-11):2095-2102.

37. Melnikov A, Mandelis A, Tolev J, Chen P, Huq S. Infrared lock-in carrierography (photocarrier radiometric imaging) of Si solar cells. *J Appl Phys*. 2010;107(11):114513.

38. Sun QM, Melnikov A, Mandelis A. Camera-based lock-in and heterodyne carrierographic photoluminescence imaging of crystalline silicon wafers. *Int J Thermodyn*. 2015;36(5-6):1274-1280.

39. Guyot-Sionnest P. Electrical transport in colloidal quantum dot films. *J Phys Chem Lett*. 2012;3(9):1169-1175.

40. Wang J, Mandelis A. Variational Reconstruction of exciton multipath deexcitation lifetime spectra in coupled PbS colloidal quantum dots. *J Phys Chem C*. 2014;118(33):19484-19491.

41. Kirchartz T, Pieters BE, Taretto K, Rau U. Mobility dependent efficiencies of organic bulk heterojunction solar cells: Surface recombination and charge transfer state distribution. *Phys Rev B*. 2009;80(3): 035334.

42. Ning Z, Zhitomirsky D, Adinolfi V, et al. Graded doping for enhanced colloidal quantum dot photovoltaics. *Adv Mater*. 2013;25(12): 1719-1723.

43. Liu M, Voznyy O, Sabatini R, et al. Hybrid organic-inorganic inks flatten the energy landscape in colloidal quantum dot solids. *Nat Mater*. 2016;16:258-263.

44. Hu L, Mandelis A, Yang Z, et al. Temperature-and ligand-dependent carrier transport dynamics in photovoltaic PbS colloidal quantum dot thin films using diffusion-wave methods. *Sol Energy Mater Sol Cells*. 2017;164:135-145.

45. Nelson J. *The physics of solar cells*. London: World Scientific Publishing Co Inc; 2003. Chapter 1.

46. Zhou S, Sun J, Zhou C, Deng Z. Comparison of recombination models in organic bulk heterojunction solar cells. *Phys B Condens Matter*. 2013;415:28-33.

47. Gaur A, Kumar P. An improved circuit model for polymer solar cells. *Prog Photovolt Res Appl*. 2014;22(9):937-948.

48. Kholmicheva N, Moroz P, Bastola E, et al. Mapping the exciton diffusion in semiconductor nanocrystal solids. *ACS Nano*. 2015;9(3): 2926-2937.

49. Chuang CH, Maurano A, Brandt RE, et al. Open-circuit voltage deficit, radiative sub-bandgap states, and prospects in quantum dot solar cells. *Nano Lett*. 2015;15(5):3286-3294.

50. Sun B, Voznyy O, Tan H, et al. Pseudohalide-exchanged quantum dot solids achieve record quantum efficiency in infrared photovoltaics. *Adv Mater*. 2017;29(27):1700749.

51. Liu M, Che F, Sun B, et al. Short-chain carboxylates promote quantitative ligand exchange for stable, efficient infrared-bandgap quantum dot inks. *J Am Chem Soc*. 2017.

52. Voznyy O, Sutherland BR, Ip AH, Zhitomirsky D, Sargent EH. Engineering charge transport by heterostructuring solution-processed semiconductors. *Nat Rev Mat*. 2017;2:17026.

53. Schilinsky P, Waldauf C, Hauch J, Brabec CJ. Simulation of light intensity dependent current characteristics of polymer solar cells. *J Appl Phys*. 2004;95(5):2816-2819.

54. Yazdani N, Bozyigit D, Yarema O, Yarema M, Wood V. Hole mobility in nanocrystal solids as a function of constituent nanocrystal size. *J Phys Chem Lett*. 2014;5(20):3522-3527.

55. Wang YX, Tseng SR, Meng HF, Lee KC, Liu CH, Horng SF. Dark carrier recombination in organic solar cell. *Appl Phys Lett*. 2008;93(13): 133501.

56. Shieh JT, Liu CH, Meng HF, Tseng SR, Chao YC, Horng SF. The effect of carrier mobility in organic solar cells. *J Appl Phys*. 2010;107(8): 084503.

57. Mandoc MM, Koster LJA, Blom PWM. Optimum charge carrier mobility in organic solar cells. *Appl Phys Lett*. 2007;90(13):133504.

58. Deibel C, Wagenpfahl A, Dyakonov V. Influence of charge carrier mobility on the performance of organic solar cells. *Phys Status Solidi RRL*. 2008;2(4):175-177.

59. Tress W, Leo K, Riede M. Optimum mobility, contact properties, and open-circuit voltage of organic solar cells: A drift-diffusion simulation study. *Phys Rev B*. 2012;85(15):155201.

60. Elumalai NK, Uddin A. Open circuit voltage of organic solar cells: an in-depth review. *Energ Environ Sci*. 2016;9(2):391-410.

61. Street RA. Carrier mobility, structural order, and solar cell efficiency of organic heterojunction devices. *Appl Phys Lett*. 2008;93(13):361.

62. Wang J, Mandelis A, Melnikov A, Hoogland S, Sargent EH. Exciton lifetime broadening and distribution profiles of PbS colloidal quantum dot thin films using frequency-and temperature-scanned photocarrier radiometry. *J Phys Chem C*. 2013;117(44): 23333-23348.

63. Rezgui K, Aloulou S, Rihani J, Oueslati M. Competition between strain and confinement effects on the crystalline quality of InAs/GaAs (001) quantum dots probed by Raman spectroscopy. *J Raman Spectrosc*. 2012;43(12):1964-1968.

64. Koster LJA, Mihailetchi VD, Blom PWM. Bimolecular recombination in polymer/fullerene bulk heterojunction solar cells. *Appl Phys Lett*. 2006;88(5):052104.
65. Choi JH, Fafarman AT, Oh SJ, et al. Bandlike transport in strongly coupled and doped quantum dot solids: a route to high-performance thin-film electronics. *Nano Lett*. 2012;12(5):2631-2638.
66. Chung DS, Lee JS, Huang J, Nag A, Ithurria S, Talapin DV. Low voltage, hysteresis free, and high mobility transistors from all-inorganic colloidal nanocrystals. *Nano Lett*. 2012;12(4):1813-1820.
67. Lee JS, Kovalenko MV, Huang J, Chung DS, Talapin DV. Band-like transport, high electron mobility and high photoconductivity in all-inorganic nanocrystal arrays. *Nat Nanotechnol*. 2011;6(6):348-352.
68. Talgorn E, Gao Y, Aerts M, et al. Unity quantum yield of photogenerated charges and band-like transport in quantum-dot solids. *Nat Nanotechnol*. 2011;6(11):733-739.
69. Gao Y, Aerts M, Sandeep CS, et al. Photoconductivity of PbSe quantum-dot solids: dependence on ligand anchor group and length. *ACS Nano*. 2012;6(11):9606-9614.
70. Ning Z, Ren Y, Hoogland S, et al. All-Inorganic colloidal quantum dot photovoltaics employing solution-phase halide passivation. *Adv Mater*. 2012;24(47):6295-6299.
71. Stadler P, Sutherland BR, Ren Y, et al. Joint mapping of mobility and trap density in colloidal quantum dot solids. *ACS Nano*. 2013;7(7):5757-5762.
72. Wang Q. Fill factor related issues in hydrogenated amorphous Si solar cells. *Sol Energy Mater Sol Cells*. 2014;129:64-69.
73. Proctor CM, Kim C, Neher D, Nguyen TQ. Nongeminate recombination and charge transport limitations in diketopyrrolopyrrole-based solution-processed small molecule solar cells. *Adv Funct Mater*. 2013;23(28):3584-3594.
74. Mandelis A, Zhang Y, Melnikov A. Statistical theory and applications of lock-in carrierographic image pixel brightness dependence on multi-crystalline Si solar cell efficiency and photovoltage. *J Appl Phys*. 2012;112(5):054505.
75. Liu J, Melnikov A, Mandelis A. Silicon solar cell electrical parameter measurements through quantitative lock-in carrierographic (photoluminescence) and thermographic imaging. *Phys Status Solidi (a)*. 2013;210(10):2135-2145.

How to cite this article: Hu L, Liu M, Mandelis A, Melnikov A, Sargent EH. Colloidal quantum dot solar cell power conversion efficiency optimization using analysis of current-voltage characteristics and electrode contact imaging by lock-in carrierography. *Prog Photovolt Res Appl*. 2017;25:1034–1050. https://doi.org/10.1002/pip.2920